

# A Global Numerical Analysis of the “Central Incisor / Local Maxillary Bone” System using a Meshless Method

S.F. Moreira<sup>\*</sup>, J. Belinha<sup>\*,†,‡</sup>, L.M.J.S. Dinis<sup>\*,†</sup> and R.M. Natal Jorge<sup>\*,†</sup>

**Abstract:** In this work the maxillary central incisor is numerically analysed with an advance discretization technique – Natural Neighbour Radial Point Interpolation Method (NNRPIM). The NNRPIM permits to organically determine the nodal connectivity, which is essential to construct the interpolation functions. The NNRPIM procedure, based uniquely in the computational nodal mesh discretizing the problem domain, allows to obtain autonomously the required integration mesh, permitting to numerically integrate the differential equations ruling the studied physical phenomenon.

A numerical analysis of a tooth structure using a meshless method is presented for the first time. A two-dimensional model of the maxillary central incisor, based on the clinical literature, is established and two distinct analyses are performed. First, a complete elasto-static analysis of the incisor/maxillary structure using the NNRPIM is evaluated and then a non-linear iterative bone tissue remodelling analysis of the maxillary bone, surrounding the central incisive, is performed. The obtained NNRPIM solutions are compared with other numerical methods solutions available in the literature and with clinical cases. The results show that the NNRPIM is a suitable numerical method to analyse numerically dental biomechanics problems.

**Keywords:** Incisor, Bone Remodelling, Meshless Method, Natural Neighbour Radial Point Interpolation Method (NNRPIM), dental biomechanics.

## 1 Introduction

In the current interdisciplinary dentistry field, the dental clinical treatment planning must account the aesthetics, the impact on function, the structure and the biology. Generally, when a large portion of the enamel covering the clinical crown

---

<sup>\*</sup> IDMEC - Institute of Mechanical Engineering, Rua Dr. Roberto Frias, 4200-465 Porto, Portugal.

<sup>†</sup> Faculty of Engineering of the University of Porto – FEUP, Rua Dr. Roberto Frias, 4200-465 Porto, Portugal.

<sup>‡</sup> Correspondent Author. E-mail: jorge.belinha@fe.up.pt

has been destroyed, the enamel layer must be replaced with an artificial crown (cap). This cemented extra coronal restoration, covering the outer surface of the clinical crown, should reproduce the morphology and contours of the damage coronal portion of a tooth, performing its function and protecting the remaining tooth structure from further damage. In the artificial crown, the most frequently used materials/combinations of materials are: metal, metal-ceramic and ceramic [1]. In this work three distinct materials are studied: feldspathic ceramic and two micro-ceramic-composites showing different viscosities. The two distinct commercial caps built with light-cured micro-ceramic-composite are the commercial caps Gradia Flow and Gradia Forte, whose material properties are usually declared by the manufacture.

The prediction of the bone tissue remodelling due to the occlusal loads is also relevant in the prosthesis placement planning and to assure the success of the associated treatment. This advanced non-linear approach provides an opportunity to optimize the prosthetic device, approaching the implant to the real human dentition [2].

The bone remodelling process was firstly empirically noticed by Wolff [3]. Within this procedure the bone tissue progressively modifies its morphology in order to adapt to any new external load. Since then, many increasingly sophisticated theoretical and numerical models have been developed, defining the stimuli as a function of strain or stress. The most popular were the models of Carter [4] and Cowin [5]. Afterwards, using the Strain Energy Density (SED) optimization criterion, Pittermann's model was proposed [6]. This model combines the bone spatial distribution adaptation with the reorientation of the material axes and the stiffness parameters. This work applies a SED based optimization algorithm to obtain the bone tissue remodelling.

The remodelling algorithm considered in this research study uses a bone tissue phenomenological law obtained from an experimental study [7], which has shown that the law governing the cortical and trabecular bone behaviour should be the same [8,9]. Thus, in this approach the bone tissue anisotropic material properties gradually vary through the model domain, respecting the proposed anisotropic material law and the lower SED regions.

Since the last thirty years the Finite Element Method (FEM) has been used to analyse the natural teeth and dental implants [10]. The simulation of dental implants mechanical behaviour presents some difficulties. In order to obtain a realistic numerical solution, the system model must consider some assumptions regarding the modelling geometry, the material properties, the boundary conditions and the interface between the bone and the implant [10]. It is important to note that the analysis of the force transfer from the occlusal material to the bone tissue is essential in order to reach the success on the implant design [10,11,12].

Despite being the FEM the most frequently used numerical method in stress analysis in both industry and science [13], this work proposes the use of an advance discretization meshless technique. Meshless methods seeking the weak form solution are more suited to solve demanding computational mechanics problems [14]. Within this class of meshless methods, one can find approximation meshless methods and interpolation meshless methods. The approximation meshless methods use in the weak form approximation test functions [15,16,17]. The most evident disadvantage of these approximation meshless methods is the lack of the Kronecker delta property. Thus, the treatment of the essential and natural boundary conditions is not as straightforward as within interpolation numerical methods [18,14,19,20]. In the literature one can find several interpolation meshless methods [21,22,23,24,25, 26].

The numerical method used in this work, the Natural Neighbour Radial Point Interpolation Method (NNRPIM), combines the radial point interpolators (RPI) with the natural neighbour geometric concept [18,27]. Although being a recent developed meshless method, the NNRPIM proved to be an efficient numerical method in several demanding applications, such as material non-linearity [28] and large-deformations [29], which can be very useful in biomechanics. The NNRPIM was also successfully extended to the dynamic transient analysis [30,31,32] and the static analysis of composite materials [33,34] and functionally graded materials [35]. The NNRPIM was successfully applied in biomechanics with very promising results regarding the micro-scale and macro-scale bone tissue remodelling analysis [8,9]. The relevance of the previous referred fields in the numerical analysis of the teeth-bone biologic structure highly increases the NNRPIM success expectations.

This preliminary and pioneer work aims to show that the NNRPIM is a suitable numerical tool capable to analyse efficiently teeth-bone biologic structures, producing high quality stress field distributions (in comparison with the FEM solution) and predicting bone tissue remodelling solutions close to real clinical cases.

This work is organized as follows. In section 2 a description of the meshless method used is presented. In section 3 the bone tissue material law is presented. The bone tissue remodelling algorithm is presented in section 4. The computer implementation of the maxillary central incisor is performed in section 5, where several elastostatic and bone tissue remodelling analyses are studied. And finally, in sections 6 and 7, the obtained results are discussed and the final remarks and conclusions are made.

## 2 The Meshless Method

In order to discretize the problem domain, the NNRPIM only requires a nodal distribution. All the other numerical structures required to solve the problem (nodal connectivity, numerical integration, shape functions, etc.) are constructed using the initial nodal distribution. Thus, being a truly meshless methods, the NNRPIM is more appropriate to discretize highly irregular domains, such as biological structures, than conventional mesh-dependent numerical approaches. Additionally, comparing the NNRPIM with other meshless methods and the FEM, it was found that the stress fields obtained with the NNRPIM are more accurate [18,27]. This section briefly presents the main features of the NNRPIM formulation.

### 2.1 NNRPIM Discretization

The first step in a NNRPIM analysis is the discretization of the problem domain  $\Omega$ , bounded by a physical boundary  $\Gamma$ , in several randomly distributed nodes  $\mathbf{N} = \{n_0, n_1, \dots, n_N\} \in \mathbb{R}^2$  with the following coordinates:  $\mathbf{X} = \{\mathbf{x}_0, \mathbf{x}_1, \dots, \mathbf{x}_N\}$  with  $\mathbf{x}_i \in \mathbb{R}^2$ , as it is represented in Figure 1(a) and (b). Then, using the natural neighbour concept [36], the Voronoï diagram of  $\mathbf{N}$  is built, which is the partition of the domain defined by  $\Omega$  in sub-regions  $V_I$ , closed and convex. Each sub-region  $V_I$  is associated with the node  $I$ ,  $n_I$ , in a way that any point in the interior of the  $V_I$  is closer to  $n_I$  than any other node  $n_J$ , where  $n_J \in \mathbf{N}$  ( $J \neq I$ ). The sub-regions  $V_k$ ,  $k = 1, \dots, N$ , are defined as “Voronoi cells” whose assemblage form the Voronoï diagram, Figure 1(c).

Afterwards, the NNRPIM uses the influence-cell concept to establish the nodal connectivity [18,27,37,20]. This numerical structure is formed by a set of nodes in the neighbourhood of an interest point  $\mathbf{x}_i$ , allowing to determine the influence-domain of that interest point  $\mathbf{x}_i$ . In Figure 1(d) it is shown an example of the the kind of influence-cells used in this work.

Additionally, after the definition of the Voronoï Diagram, Figure 1(c), it is possible to construct a node dependent integration mesh, required to numerically integrate the differential equation ruling the studied physical phenomenon. The area of each Voronoï cell,  $A^{V_j}$ , of each node  $\mathbf{x}_j \in \mathbf{X}$ , is subdivided in  $k$  sub-areas  $A_i^{V_j}$ , being  $A^{V_j} = \sum_{i=1}^k A_i^{V_j}$ . The distribution of the integration points inside each sub-area  $A_i^{V_j}$ , following the Gauss-Legendre quadrature rule, permits to obtain the integration mesh for the Voronoï cell  $V_j$ . Repeating the process for the  $N$  Voronoï cells discretizing the problem domain it is possible to obtain the domain integration mesh, being  $A^\Omega = \sum_{j=1}^N \sum_{i=1}^k A_i^{V_j}$ . In this work only one quadrature point was applied in each one of the divisions.

It is important to mention that with this integration scheme it is possible to obtain

a numerical integration mesh total dependent of the nodal mesh. Complete theoretical descriptions and mathematical proofs of the NNRPIM formulation can be found in the literature [18,20].

### 2.2 Radial Point Interpolators

Within the NNRPIM the interpolation functions are constructed using the Radial Point Interpolators (RPI). The classical RPI require a radial basis function (RBF) and a complete polynomial basis [38], however previous works on the NNRPIM showed that if the shape parameters of the RBF are chosen carefully the polynomial basis can be removed from the formulation and substituted by a unity basis [18,20], permitting to enhance the method computational efficiency.

A function  $u(\mathbf{x})$  defined in the domain  $\Omega \subset \mathbb{R}^d$  is assumed. Additionally it is considered an interest point  $\mathbf{x}_I \in \Omega$ , possessing an influence-cell containing  $n$  nodes,  $\mathbf{X}_I = \{\mathbf{x}_1, \mathbf{x}_2, \dots, \mathbf{x}_n\} \in \Omega$  with  $\mathbf{x}_i \in \mathbb{R}^d$  and  $\mathbf{X}_I \in \mathbf{X}$ . It is assumed that only the nodes within the influence-cell of the interest point  $\mathbf{x}_I$  have effect on  $u(\mathbf{x}_I)$ . The value of function  $u(\mathbf{x}_I)$  at the point of interest  $\mathbf{x}_I$  is defined by,

$$u(\mathbf{x}_I) = \sum_{i=1}^n [R_i(\mathbf{x}_I) \cdot a_i(\mathbf{x}_I)] + C_u \cdot b(\mathbf{x}_I) = \mathbf{R}(\mathbf{x}_I) \cdot \mathbf{a}(\mathbf{x}_I) + C_u \cdot b(\mathbf{x}_I) \quad (1)$$

where  $R_i(\mathbf{x}_I)$  is the RBF and  $a_i(\mathbf{x}_I)$  are non-constant coefficients of  $R_i(\mathbf{x}_I)$ . The parameter  $C_u$  is the unity basis, being  $C_u = 1$  and  $b(\mathbf{x}_I)$  is a non-constant coefficient of  $C_u$ . Within the RBF the variable is defined by the distance  $r_{Ii}$  between the relevant node  $\mathbf{x}_I$  and the neighbour node  $\mathbf{x}_i$ ,  $r_{Ii} := |\mathbf{x}_i - \mathbf{x}_I|$ . In the work of Wang and Liu [38] several RBFs are well studied and developed. Proposed initially by Hardy [39], in this work it is used the Multiquadric (MQ) function,  $R_i(\mathbf{x}_I) = R(r_{Ii}) = (r_{Ii}^2 + c^2)^p$ , in which  $c$  and  $p$  are two shape parameters. It was found that  $c$  should be close to zero,  $c \cong 0$ , and  $p$  should be close to one,  $p \cong 1$ . The optimal shape parameter  $c$  and  $p$  values obtained in [18,20] are universal, meaning that both can be used in the constructing of the interpolation functions regardless the studied phenomenon [18,27,37,20]. Applying equation (1) to each node inside the influence-cell domain, considering sequentially each node as the interest point, and including an extra equation  $\sum_{i=1}^n a_i(\mathbf{x}_I) = 0$  to guarantee an unique solution [40], it is possible to obtain the following equations system,

$$\begin{bmatrix} u_1 \\ u_2 \\ \vdots \\ u_n \\ 0 \end{bmatrix} = \begin{bmatrix} R(r_{11}) & R(r_{12}) & \cdots & R(r_{1n}) & 1 \\ R(r_{21}) & R(r_{22}) & \cdots & R(r_{2n}) & 1 \\ \vdots & \vdots & \ddots & \vdots & \vdots \\ R(r_{n1}) & R(r_{n2}) & \cdots & R(r_{nn}) & 1 \\ 1 & 1 & \cdots & 1 & 0 \end{bmatrix} \begin{bmatrix} a_1(\mathbf{x}_I) \\ a_2(\mathbf{x}_I) \\ \vdots \\ a_n(\mathbf{x}_I) \\ b(\mathbf{x}_I) \end{bmatrix} \Leftrightarrow \begin{bmatrix} \mathbf{u}_s \\ 0 \end{bmatrix} = \begin{bmatrix} \mathbf{R} & C_u \\ C_u & 0 \end{bmatrix} \begin{bmatrix} \mathbf{a} \\ b \end{bmatrix} \quad (2)$$

being  $\mathbf{u}_s = \{u_1 \ u_2 \ \dots \ u_n\}^T$  the vector for the nodal function values for the nodes on the influence-cell. Therefore, it is possible to obtain the non-constant coefficients from equation (2),

$$\begin{bmatrix} \mathbf{a} \\ b \end{bmatrix} = \begin{bmatrix} \mathbf{R} & \mathbf{C}_u \\ \mathbf{C}_u & 0 \end{bmatrix}^{-1} \begin{bmatrix} \mathbf{u}_s \\ 0 \end{bmatrix} \Rightarrow \begin{bmatrix} \mathbf{a} \\ b \end{bmatrix} = \mathbf{M}^{-1} \begin{bmatrix} \mathbf{u}_s \\ 0 \end{bmatrix} \quad (3)$$

Substituting in equation (1) the result from equation (3), it is possible to obtain the interpolation function  $\varphi(\mathbf{x}_I)$  for an interest point  $\mathbf{x}_I$ ,

$$u(\mathbf{x}_I) = \{R_1(\mathbf{x}_I) \ R_2(\mathbf{x}_I) \ \dots \ R_n(\mathbf{x}_I) \ C_u\} \mathbf{M}^{-1} \mathbf{u}_s = \varphi(\mathbf{x}_I) \mathbf{u}_s \quad (4)$$

The partial derivative of  $\varphi(\mathbf{x}_I)$  with respect to a generic variable  $\xi$  is defined as,

$$\varphi_{,\xi}(\mathbf{x}_I) = \{R_1(\mathbf{x}_I) \ R_2(\mathbf{x}_I) \ \dots \ R_n(\mathbf{x}_I) \ C_u\}_{,\xi} \mathbf{M}^{-1} \quad (5)$$

Notice that being  $C_u$  constant  $C_{u,\xi} = 0$ . The partial derivatives of the MQ-RBF with respect to a generic variable  $\xi$  are obtained with,

$$R_{,\xi}(r_{ij}) = 2p (r_{ij}^2 + c^2)^{p-1} (\xi_j - \xi_i) \quad (6)$$

In the literature [18,24,38,20] it is possible to find complete studies on the RPI interpolation functions: construction procedure and properties.

### 2.3 Discrete Equation System

Consider a closed domain  $\Omega$  bonded by  $\Gamma$ . The equilibrium equations are expressed by:  $\nabla \boldsymbol{\sigma} + \mathbf{b} = 0$  in  $\Omega$ , where  $\nabla$  is the gradient vector,  $\boldsymbol{\sigma}$  the Cauchy stress tensor and  $\mathbf{b}$  the set of external forces applied to the body. Applying the Galerkin weak form, the following expression is obtained,

$$\psi = \int_{\Omega} \delta \boldsymbol{\varepsilon}^T \boldsymbol{\sigma} d\Omega - \int_{\Omega} \delta \mathbf{u}^T \mathbf{b} d\Omega - \int_{\Gamma} \delta \mathbf{u}^T \mathbf{t} d\Gamma = 0 \quad (7)$$

where  $\mathbf{t}$  is the vector of external forces applied to the natural boundary  $\Gamma$ ,  $\boldsymbol{\varepsilon}$  is the strain vector and  $\mathbf{u}$  is the displacement field vector. The strain vector can be represented as  $\boldsymbol{\varepsilon} = \mathbf{L}\mathbf{u}$ . In this work only small deformations and elasto-static assumptions are considered. Therefore, with the Hooke Law it is possible to obtain the stress field  $\boldsymbol{\sigma} = \mathbf{c}\boldsymbol{\varepsilon} = \mathbf{c}\mathbf{L}\mathbf{u}$ , being  $\mathbf{L}$  is a differential operator depending on the deformation theory and  $\mathbf{c}$  is the material constitutive matrix, which can be obtained

inverting the compliance elasticity matrix,  $\mathbf{c} = \mathbf{s}^{-1}$ . The compliance elasticity matrix  $\mathbf{s}$  for the general anisotropic material case is defined in equation (8), respectively for the plane stress and plane strain formulations.

$$\mathbf{s}_{plane\ stress} = \begin{bmatrix} \frac{1}{E_{11}} & -\frac{\nu_{21}}{E_{22}} & 0 \\ -\frac{\nu_{12}}{E_{11}} & \frac{1}{E_{22}} & 0 \\ 0 & 0 & \frac{1}{G_{12}} \end{bmatrix}$$

and

$$\mathbf{s}_{plane\ strain} = \begin{bmatrix} \frac{1-\nu_{31}\nu_{13}}{E_{11}} & -\frac{\nu_{12}+\nu_{31}\nu_{23}}{E_{22}} & 0 \\ -\frac{\nu_{12}+\nu_{32}\nu_{13}}{E_{11}} & \frac{1-\nu_{32}\nu_{23}}{E_{22}} & 0 \\ 0 & 0 & \frac{1}{G_{12}} \end{bmatrix}$$

being  $E_{ij}$  the elasticity modulus,  $\nu_{ij}$  material Poisson coefficient and  $G_{ij}$  the distortion modulus in material direction  $i$  and  $j$ . It is possible to align the constitutive matrix  $\mathbf{c}$  with a new material referential  $Ox^*y^*$  defined by  $\mathbf{i}^* = \{i_x^*, i_y^*\}$  and  $\mathbf{j}^* = \{j_x^*, j_y^*\} = \{-i_y^*, i_x^*\}$ , which are the versors of the new material referential. Thus,

$$\mathbf{c}^* = \mathbf{T}^T \mathbf{c} \mathbf{T} \tag{9}$$

where the transformation matrix  $\mathbf{T}$  is defined by,

$$\mathbf{T} = \begin{bmatrix} \cos^2 \beta & \sin^2 \beta & -\sin 2\beta \\ \sin^2 \beta & \cos^2 \beta & \sin 2\beta \\ \sin \beta \cdot \cos \beta & -\sin \beta \cdot \cos \beta & \cos^2 \beta - \sin^2 \beta \end{bmatrix} \tag{10}$$

The angle  $\beta$  is the angle between the original material axis  $Ox$  and the new material axis  $Ox^*$ :  $\beta = \cos^{-1}(\mathbf{i} \cdot \mathbf{i}^*)$ . Substituting  $\boldsymbol{\varepsilon} = \mathbf{L}\mathbf{u}$  in the first term of equation (7) and considering equation (4) the following expression is obtained,

$$\int_{\Omega} \delta(\mathbf{L}\boldsymbol{\varphi}_I(\mathbf{x})\mathbf{u}_I)^T \mathbf{c} (\mathbf{L}\boldsymbol{\varphi}_I(\mathbf{x})\mathbf{u}_I) d\Omega = \int_{\Omega} \delta(\mathbf{B}\mathbf{u}_I)^T \mathbf{c} (\mathbf{B}\mathbf{u}_I) d\Omega = \delta\mathbf{u}_I^T \left[ \int_{\Omega} \delta\mathbf{B}^T \mathbf{c} \mathbf{B} d\Omega \right] \mathbf{u}_I \tag{11}$$

Repeating the procedure for the second and third term of the right side of equation (7), it is obtained  $\int_{\Omega} \delta\mathbf{u}_I^T \mathbf{b} d\Omega = \delta\mathbf{u}_I^T \int_{\Omega} \mathbf{H}\mathbf{b} d\Omega$  and  $\int_{\Gamma} \delta\mathbf{u}_I^T \mathbf{t} d\Gamma = \delta\mathbf{u}_I^T \int_{\Gamma} \mathbf{H}\mathbf{t} d\Gamma$ . For the  $n$  nodes constituting the influence-cell of interest point  $x_I$ , matrices  $\mathbf{B}$  and  $\mathbf{H}$  can be defined as,

$$\mathbf{B} = \begin{bmatrix} \frac{\partial \varphi_1(\mathbf{x}_I)}{\partial x} & 0 & \frac{\partial \varphi_2(\mathbf{x}_I)}{\partial x} & 0 & \dots & \frac{\partial \varphi_n(\mathbf{x}_I)}{\partial x} & 0 \\ 0 & \frac{\partial \varphi_1(\mathbf{x}_I)}{\partial y} & 0 & \frac{\partial \varphi_2(\mathbf{x}_I)}{\partial y} & \dots & 0 & \frac{\partial \varphi_n(\mathbf{x}_I)}{\partial y} \\ \frac{\partial \varphi_1(\mathbf{x}_I)}{\partial y} & \frac{\partial \varphi_1(\mathbf{x}_I)}{\partial x} & \frac{\partial \varphi_2(\mathbf{x}_I)}{\partial y} & \frac{\partial \varphi_2(\mathbf{x}_I)}{\partial x} & \dots & \frac{\partial \varphi_n(\mathbf{x}_I)}{\partial y} & \frac{\partial \varphi_n(\mathbf{x}_I)}{\partial x} \end{bmatrix} \tag{12}$$

and

$$\mathbf{H}^T = \begin{bmatrix} \varphi_1(\mathbf{x}_I) & 0 & \varphi_2(\mathbf{x}_I) & 0 & \cdots & \varphi_n(\mathbf{x}_I) & 0 \\ 0 & \varphi_1(\mathbf{x}_I) & 0 & \varphi_2(\mathbf{x}_I) & \cdots & 0 & \varphi_n(\mathbf{x}_I) \end{bmatrix} \quad (13)$$

With back substitution in equation (7) it is possible to obtain the following linear system of equations:  $\boldsymbol{\psi} = \delta \mathbf{U}^T [\mathbf{K}\mathbf{U} - \mathbf{F}] = 0$ , which can be represented in the following matrix form:  $\mathbf{K}\mathbf{U} = \mathbf{F}$ , where  $\mathbf{K}$  is stiffness matrix,  $\mathbf{U}$  is the displacement field vector and  $\mathbf{F}$  is the vector of applied forces. Since the RPI shape function possesses the delta Kronecker property, the essential boundary conditions can be directly applied in the stiffness matrix [18,20].

After the determination of the displacement field using  $\mathbf{K}\mathbf{U} = \mathbf{F}$ , the strain field is obtained with  $\boldsymbol{\varepsilon} = \mathbf{L}\mathbf{u}$  and then, considering the Hooke Law, it is possible to determine the stress field,  $\boldsymbol{\sigma} = \mathbf{c}\boldsymbol{\varepsilon}$ . Afterwards it is possible to obtain the three principal stresses  $\sigma_i$  for each interest point  $\mathbf{x}_I$ ,  $\det(\boldsymbol{\sigma} - \sigma_i \mathbf{I}) = 0$ , and the three principal directions  $\mathbf{n}_i$ :  $(\boldsymbol{\sigma} - \sigma_i \mathbf{I}) \mathbf{n}_i = 0$ , being  $\boldsymbol{\sigma}$  the Cauchy stress tensor and  $\mathbf{I}$  the identity matrix. The von Mises effective stress field can be obtained using the three principal stresses  $\sigma_i$ ,

$$\bar{\sigma} = \sqrt{\frac{1}{2} \left( (\sigma_1 - \sigma_2)^2 + (\sigma_2 - \sigma_3)^2 + (\sigma_3 - \sigma_1)^2 \right)} \quad (14)$$

The strain energy density (SED) field for the considered load case is determined using the stress field and the strain field. The SED for the interest point  $\mathbf{x}_I$  is obtained with,

$$U(\mathbf{x}_I) = \frac{1}{2} \int_{\Omega_I} \boldsymbol{\sigma}(\mathbf{x}_I)^T \boldsymbol{\varepsilon}(\mathbf{x}_I) d\Omega_I \quad (15)$$

### 3 Bone tissue material law

Commonly, the bone tissue is divided in two categories: the cortical bone, presenting a higher apparent density; and the trabecular bone, showing a considerably smaller apparent density. Although, from the micro-scale point of view, both types show the same molecular arrangement, from the macro-scale perspective the global mechanical behaviour differs. Several published studies show that the bone mechanical properties depend on the bone composition and on the bone apparent density [41-46]. One of the first works to consider the bone orthotropic behaviour was the work of Lotz [47]. The phenomenological mathematical laws proposed by Lotz permit to obtain the elasticity modulus and the ultimate compressive stress, for both cortical and trabecular bone, in the axial and transversal direction using only the apparent density,  $\rho_{app}$ , as variable. More recently, the experimental study performed by Zioupos et al. [7] reinforced the idea that the apparent density is a

central property of bone tissue. Following Zioupos work, Belinha et al. [8,9] proposed a new orthotropic mathematical law governing the mechanical behaviour of the bone tissue, correlating the apparent density with the bone tissue mechanical properties, unifying in the same mathematical law the cortical and trabecular bone tissue. The curve proposed by Belinha et al. [8,9] for the elasticity modulus in the axial direction possesses a 95% correlation with Zioupos experimental data,

$$\begin{cases} E_{axial} = \sum_{j=0}^3 a_j \cdot (\rho_{app})^j & \text{if } \rho_{app} \leq 1.3g/cm^3 \\ E_{axial} = \sum_{j=0}^3 b_j \cdot (\rho_{app})^j & \text{if } \rho_{app} > 1.3g/cm^3 \end{cases} \quad (16)$$

The curve for elasticity modulus in the transversal direction was obtained using the Lotz’s curves [47] and is determined with,

$$E_{trans} = \sum_{j=0}^3 c_j \cdot (\rho_{app})^j \quad (17)$$

being  $E_i$  the elasticity modulus in direction  $i$ . Using the same methodology, Belinha et al. [8,9] combined in a single curve the cortical and trabecular mathematical laws proposed by Lotz [47] for the ultimate compression stress  $\sigma_i^c$  in both axial and transversal directions,

$$\sigma_{axial}^c = \sum_{j=0}^3 d_j \cdot (\rho_{app})^j \quad (18)$$

$$\sigma_{trans}^c = \sum_{j=0}^3 e_j \cdot (\rho_{app})^j \quad (19)$$

Equations (16) to (19) are expressed in *MPa* and the apparent density  $\rho_{app}$  is expressed in  $g/cm^3$ . The coefficients  $a_j, b_j, c_j, d_j$  and  $e_j$  are presented in Table 1.

Table 1: Curve coefficients

Coefficient	$j=0$	$j=1$	$j=2$	$j=3$
$a_j$	0.000E+00	7.216E+02	8.059E+02	0.000E+00
$b_j$	-1.770E+05	3.861E+05	-2.798E+05	6.836E+04
$c_j$	0.000E+00	0.000E+00	2.004E+03	-1.442E+02
$d_j$	0.000E+00	0.000E+00	2.680E+01	2.035E+01
$e_j$	0.000E+00	0.000E+00	2.501E+01	1.247E+00

## 4 Bone tissue remodelling

In this work it is assumed that the mechanical stimulus is the principal driving force triggering the bone tissue remodelling process. The mechanical stimulus, which can be described by the stress field and/or the strain field, permits to determine iteratively the local density and the material orientation. The remodelling algorithm used in this work [8,9] can be considered as an adaptation of Carter's model for natural neighbour meshless methods.

### 4.1 Remodelling methodology

Here, the bone tissue remodelling is numerically described by a nonlinear differential equation  $\rho_{app}(\mathbf{x}, t) : \mathbb{R}^{d+1} \mapsto \mathbb{R}$ . This temporal-spatial functional, discretized along the one-dimensional temporal line and the  $d$ -dimensional space, is minimized with respect to time,

$$\frac{\partial \rho_{app}(\mathbf{x}, t)}{\partial t} \simeq \frac{\Delta \rho_{app}(\mathbf{x}, t)}{\Delta t} = \frac{(\rho_{app}^{model})_{t_{j+1}} - (\rho_{app}^{model})_{t_j}}{t_{j+1} - t_j} = 0 \quad (20)$$

Notice that the NNRPIM procedure requires that the  $d$ -dimensions spatial domain must be discretized in  $N$  nodes:  $\mathbf{X} = \{\mathbf{x}_1, \mathbf{x}_2, \dots, \mathbf{x}_N\} \in \Omega$ . Additionally, using  $\mathbf{X}$ , it is possible to determine the  $Q$  interest points:  $\mathbf{Q} = \{\mathbf{x}_1, \mathbf{x}_2, \dots, \mathbf{x}_Q\} \in \Omega$ , being  $\mathbf{x}_i \in \mathbb{R}^d$  and  $\mathbf{Q} \cap \mathbf{X} = \emptyset$ .

As equation (20) shows, the temporal domain is discretized in iterative fictitious time steps  $t_j \in \mathbb{R}$ , with  $j \in \mathbb{N}$ , and the medium apparent density for the complete model domain, at a fictitious time  $t_j$ , is defined by  $(\rho_{app}^{model})_{t_j}$ . Within the same iterative fictitious time step, the medium apparent density of the model,  $\rho_{app}^{model}$ , can be determined with,

$$\rho_{app}^{model} = Q^{-1} \sum_{i=1}^Q (\rho_{app})_i \quad (21)$$

In which  $(\rho_{app})_I$  is the infinitesimal apparent density on interest point  $\mathbf{x}_I$  defined by the functional  $\rho_I = g(\boldsymbol{\sigma}_I)$ ,

$$g(\boldsymbol{\sigma}_I) = \min(\{\boldsymbol{\sigma}_1^{-1}(\rho_I), \boldsymbol{\sigma}_2^{-1}(\rho_I), \boldsymbol{\sigma}_3^{-1}(\rho_I)\}) \quad (22)$$

Notice that  $\boldsymbol{\sigma}_k$  are the three principal stresses obtained in the interest point  $\mathbf{x}_i$  and  $\boldsymbol{\sigma}_k^{-1}(\rho_I)$  are the inverse functions of  $\boldsymbol{\sigma}_k(\rho_I)$  defined in equations (18) and (19). Thus, for the principal stress  $\boldsymbol{\sigma}_1$ , it is possible to obtain the following expression,

$$\boldsymbol{\sigma}_1^{-1}(\rho_I) = \boldsymbol{\sigma}_{axial}^{-1}(\rho_I) = \rho_{axial} = 8.14 \times 10^{-4} f_1(\boldsymbol{\sigma}_1) + \frac{235.3}{f_1(\boldsymbol{\sigma}_1)} - 0.439 \quad (23)$$

and for the remaining principal stresses  $\sigma_k$  with  $k = \{2, 3\}$ ,

$$\sigma_k^{-1}(\rho_I) = \sigma_{trans}^{-1}(\rho_I) = \rho_{trans} = 1.34 \times 10^{-3} f_2(\sigma_k) + \frac{3.34 \times 10^4}{f_2(\sigma_k)} - 0.669 \quad (24)$$

the functions  $f_1(\sigma_1) : \mathbb{C} \mapsto \mathbb{R}$  and  $f_2(\sigma_k) : \mathbb{C} \mapsto \mathbb{R}$  are defined as,

$$f_1(\sigma_1) = Re \left( -1.54 \times 10^8 + 4.47 \times 10^7 \sigma_1 + 2.44 \times 10^3 \sqrt{-2.31 \times 10^9 \sigma_1 + 3.35 \times 10^9 \sigma_1^2} \right) \quad (25)$$

$$f_2(\sigma_k) = Re \left( -1.25 \times 10^{11} + 1.68 \times 10^8 \sigma_k + 1.49 \times 10^4 \sqrt{-1.88 \times 10^{11} \sigma_k + 1.26 \times 10^8 \sigma_k^2} \right) \quad (26)$$

The remodelling process suggested in this work is local, therefore the expressions presented in equations (23) and (24) are only applied to the interest point  $\mathbf{x}_I$  with SED values belonging to the following interval,

$$U(\mathbf{x}_I) \in [U_m, U_m + \alpha \cdot \Delta U \cup U_M - \beta \cdot \Delta U, U_M], \forall U(\mathbf{x}_I) \in \mathbb{R} \quad (27)$$

being  $U_m = \min(\mathbf{U})$  and  $U_M = \max(\mathbf{U})$  and  $\Delta U = U_M - U_m$ . The SED field of the problem domain is defined by:  $\mathbf{U} = \{U(\mathbf{x}_1)U(\mathbf{x}_2) \cdots U(\mathbf{x}_Q)\}$ . The parameters  $\alpha$  and  $\beta$  define the growth rate and the decrease rate of the apparent density. The remodelling equilibrium is achieved when,

$$\frac{\Delta \rho}{\Delta t} = 0 \quad \vee \quad (\rho_{app}^{model})_{t_j} = \rho_{app}^{control} \quad (28)$$

The values of parameters  $\alpha$  and  $\beta$  and the value of the control apparent density  $\rho_{app}^{control}$  vary with the analysed problem.

#### 4.2 Remodelling algorithm description

The implemented iterative remodelling process, a forward Euler scheme, is presented in Figure 2.

First, the geometry and the most relevant biological structures are identified from the available medical images. Then, it is possible to discretize the problem domain using the NNRPIM procedure. The nodal mesh is constructed,  $\mathbf{X} \in \Omega$ , and the respective Voronoï diagram is obtained. Afterwards, the nodal connectivity is determined and the integration mesh,  $\mathbf{Q} \in \Omega \wedge \mathbf{Q} \cap \mathbf{X} = \emptyset$ , is constructed. The discretization procedure is concluded with the construction of the interpolation functions and the enforcement of the essential and natural boundary conditions. Ending

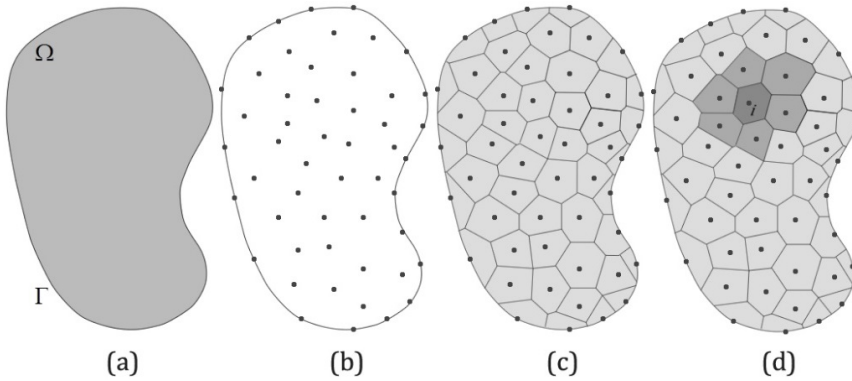


Figure 1: (a) Problem domain; (b) Discretization of the problem domain in several nodes; (c) Obtained Voronoï diagram; (d) influence-cell.

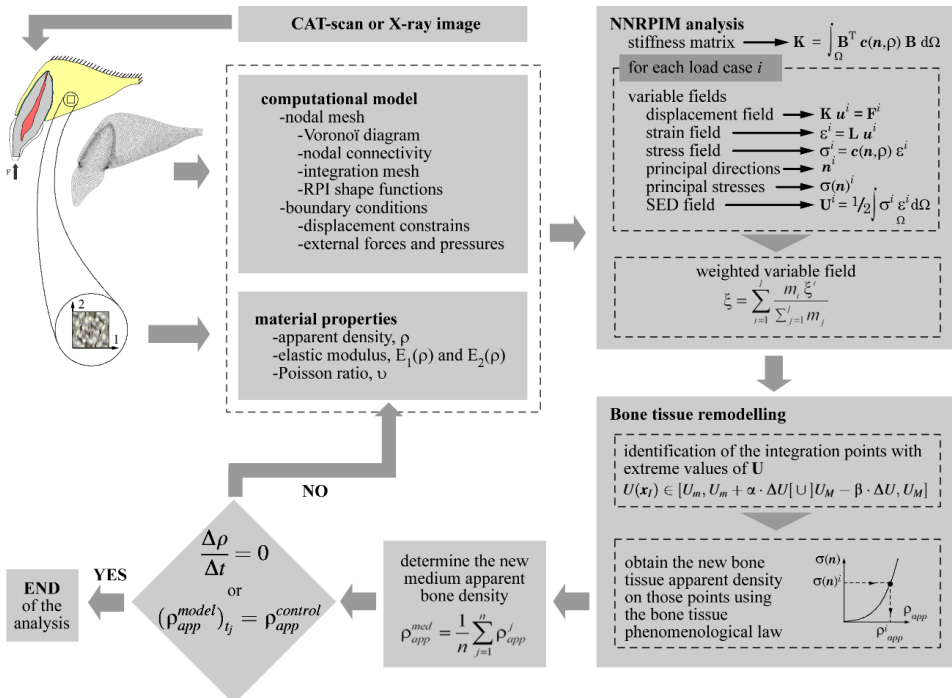


Figure 2: Bone tissue remodelling algorithm

the pre-processing phase, the material properties are allocated to the respective domain areas. Then, the iterative remodelling algorithm can be initiated.

The iterative loop begins with a trial linear analysis of the problem. The main purpose of this first step is to obtain the principal directions of the stress field in each integration point. With the principal directions field it is possible to align for each integration point the material constitutive matrix with the principal direction of the respective maximum principal stress, equation (9). Thus, in this first step of the iterative loop,  $j = 0$ , it is considered an initial isotropic constitutive elastic matrix, obtained with the compliance matrix presented in equation (8). The local stiffness matrix for each integration point is constructed, equation (11), and afterwards assembled into a global stiffness matrix  $\mathbf{K}_j$ .

The remodelling algorithm presented in this work permits to consider simultaneously several load cases,  $\mathbf{f}_j^k$ . It is possible to determine the displacement field of each load case,  $\mathbf{u}_j^k = \mathbf{K}_j^{-1} \mathbf{f}_j^k$ , and then to establish the respective strain field  $\boldsymbol{\varepsilon}_j^m$  and stress field  $\boldsymbol{\sigma}_j^m$ . Using the stress field  $\boldsymbol{\sigma}_j^m$  the principal stresses,  $\boldsymbol{\sigma}(\mathbf{n})_j^m$ , and directions,  $\mathbf{n}_j^m$ , are obtained, as well as the SED field  $\mathbf{U}_j^m$ , equation (15).

This procedure is then repeated for each load case considered and, in the end, the variable fields obtained for each load case are weighted using equation (29). Considering a generic variable field  $\xi$  (which can be assumed as the displacement field, the strain field, the stress field, etc.), the final weighted field value is determined by an appropriate superposition of a number of relevant discrete load cases,  $l$ , weighted according to the corresponding number of load cycles,  $m$ .

$$\xi_j = \sum_{k=1}^l \frac{m^{(k)} \xi_j^k}{\sum_{s=1}^l m^{(s)}} \quad (29)$$

Afterwards, the interest points presenting the SED values within the range indicated in equation (27) are identified and subjected to a density remodelling process. Being this a local remodelling process, all the other interest points outside the range governed by equation (27) maintain the previous density.

Using the weighted principal stress field of the interest points presenting lower SED values (determined using equation (29)) it is possible to determine with equation (22) the individual new apparent density of these interest points. With the new apparent density established the process moves forward the next iteration step.

Considering the updated apparent density field, the material properties are updated in each interest point using equations (16) and (17). Then, the constitutive elasticity matrix, defined in each interest point, is oriented using equation (9) applying the principal directions obtained in the previous iteration step. This procedure permits to align iteratively the material properties with the actualized load path. The

process stops when the medium apparent density of the model,  $\rho_{app}^{model}$ , reaches a controlled value,  $\rho_{app}^{control}$ , or if two consecutive iteration steps present the same medium apparent density,  $\Delta\rho/\Delta t = 0$ . The control value is determined by the user, based on clinical observations.

The inclusion of the NNRPIM meshless method in the remodelling analysis is an asset and not just another way to obtain the stress and the strain field, since the accuracy of the remodelling algorithm depends on the accuracy of the used numerical method.

Notice that, although the constitutive material matrix of each interest point is oriented with the principal directions obtained in the previous iteration step, only a few interest points optimize their apparent density in each iteration step. Just these few interest points with lower SED or higher SED, equation (27), are subject to the density remodelling process, all the others maintain the previous density. With this approach, the material properties orientation is continuously optimized and only a small fraction of bone material have its density actualized at each time.

### 4.3 NNRPIM results interpretation

After the discretization of the solid domain  $\Omega \subset \mathbb{R}^d$  with an unstructured nodal distribution,  $\mathbf{X} \in \Omega$ , the Voronoï diagram is constructed  $\mathbf{V} = \{V_1, V_2, \dots, V_N\}$ , being  $\Omega = \bigcup_{i=1}^N V_i$ . Recall that the integration points  $\mathbf{Q} \in \Omega$ , discretizing the problem domain, are determined sequentially for each Voronoï cell  $V_i$ , which will permit to produce  $k$  integration points, being:  $\mathbf{Q}_{V_i} = \{\mathbf{x}_1, \mathbf{x}_2, \dots, \mathbf{x}_k\} \in \mathbf{Q}$  and  $\mathbf{Q}_{V_i} \subset V_i$ , Figure 3(a).

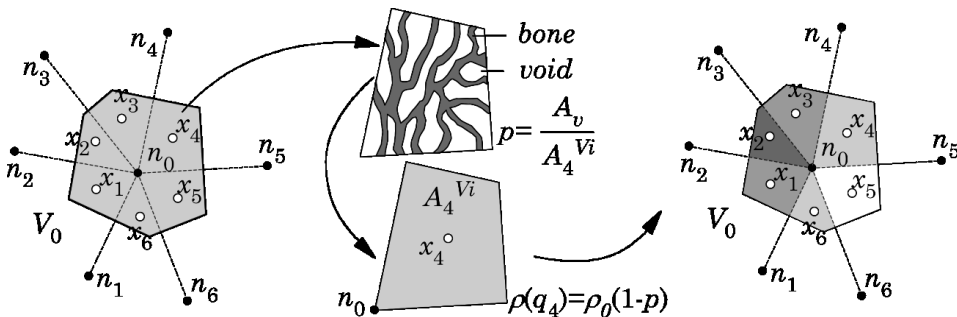


Figure 3: (a) Voronoï cell with the quadrature points. (b) Theoretical trabecular architecture of the sub-cell and homogenized apparent density. (c) Voronoï cell with the integration points homogenized apparent densities.

The local apparent density,  $\rho(\mathbf{x}_J)_{app}$ , of every integration point  $\mathbf{x}_J$ , is obtained in

the end of each iteration step. Recall that the smallest dimensional partition of the domain is the infinitesimal subdivision of each Voronoï cell  $V_i$  – the sub-cells  $A_J^{V_i}$ . The Voronoï cell infinitesimal subdivision  $A_J^{V_i}$  is numerically represented by the respective integration point  $\mathbf{x}_J$ . Since the infinitesimal subdivision  $A_J^{V_i}$  is discretised with only one point (the integration point  $\mathbf{x}_J$ ) inside the infinitesimal subdivision  $A_J^{V_i}$ , it is not possible to obtain the detailed microscale trabecular arrangement represented in Figure 3(b), in which the bone volume,  $A_b$ , and the void volume,  $A_v$ , are clearly defined. Instead, for each  $A_J^{V_i}$  it is only possible to obtain the volume porosity,  $p(\mathbf{x}_J)$ , and then the local apparent density  $\rho(\mathbf{x}_J)_{app} = \rho_0(1 - p(\mathbf{x}_J))$ , being  $\rho_0 = 2.1g/cm^3$  the compact bone density, Figure 3(b). As it is understandable, decreasing the size of the infinitesimal subdivisions it will permit to increase the detail of the analysis, however it will increase also the computational cost. As represented in Figure 3(c) each integration point will probably present a distinct local apparent density. Additionally, it is possible to obtain the local apparent density of each field node  $\mathbf{x}_i$ ,

$$\rho(\mathbf{x}_i)_{app} = \frac{\sum_{J=1}^k \widehat{w}_J \cdot \rho(\mathbf{x}_J)_{app}}{\sum_{J=1}^k \widehat{w}_J} \quad (30)$$

where  $\widehat{w}_J$  is the integration weight of an integration point  $\mathbf{x}_J$  belonging to the Voronoï cell  $V_i$  of the field node  $\mathbf{x}_i$ . Thus, the local apparent density field can be defined directly on the nodes. This direct process is only possible due to the unique characteristics of the NNRPIM.

In this work, the results showing the evolution of the trabecular architecture are presented as grey tone isomaps, in which the dark-grey colour represents the considered maximum apparent density  $\rho_0 = 2.1g/cm^3$  and the white colour represents the minimum apparent density  $\rho_0 = 0.1g/cm^3$  admitted in the analysis. All the other grey tones in the middle represent transitional apparent densities. In each isomap presented in this work it is also indicated the domain medium apparent density, which is obtained applying equation (21). Figure 4 presents an example of an apparent density field obtained with the NNRPIM bone tissue remodelling analysis. Apparently, the result obtained for a medium apparent density  $\rho_0 = 1.2g/cm^3$  indicates a well-defined trabecular arrangement. However, as it is perceptible, the presented trabecular arrangement is dependent on the domain discretization. If more nodes were used in the analysis it would be possible to obtain a more accurate trabecular architecture.

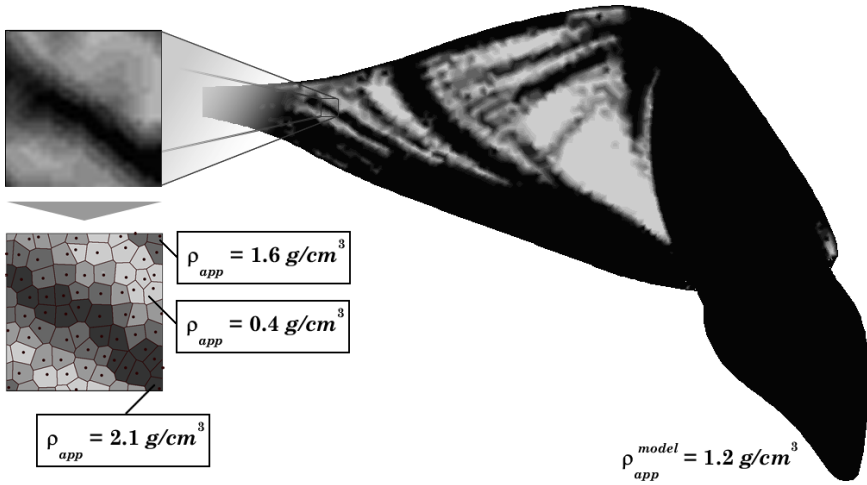


Figure 4: Isomap representing the trabecular architecture of the maxillary bone

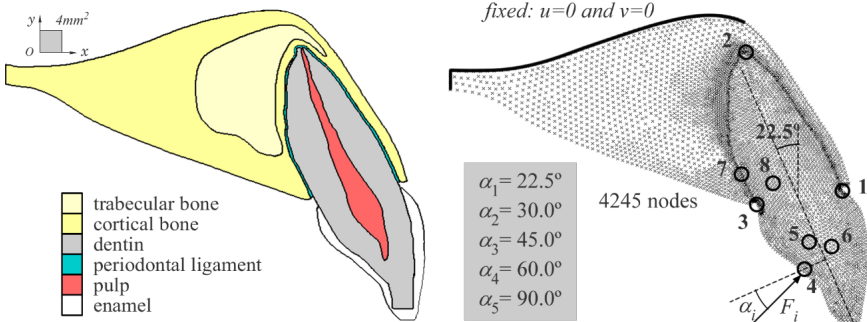


Figure 5: (a) Maxillary central incisive set for the two dimensional analysis. (b) Nodal mesh and considered essential and natural boundary conditions.

## 5 Results

### 5.1 Numerical model

In this work the used computational model of the maxillary central incisor was based in the computerized axial tomography (CAT) scan performed by Poiate et al. [48]. The problem domain and the main biologic structure considered are shown in Figure 5(a). The problem domain was discretized in an irregular nodal mesh with 4245 nodes, represented in Figure 5(b), respecting the domain differentiation between the biologic structures indicated in Figure 5(a). In this work, all the presented numerical analysis are performed considering the plane strain assumption [48].

As suggested in the literature [48], in the model upper domain boundary the nodal displacements are blocked in both directions, Figure 5(b). Regarding the natural boundary conditions, the literature [48,49] suggests the five loads  $F_i$  presented in Figure 5(b), relatively oriented to the incisor longitudinal middle axis with correspondent angles  $\alpha_i$ .

In order to compare the obtained NNRPIM results for the distinct studies, eight interest regions of the model were considered, Figure 5(b). In the indicated regions stress concentrations are expected, caused by the applied load and the model essential boundary conditions. In regions 1, 4, 6 and 8 are expected compressive stresses and tensile stresses in regions 2, 3, 5 and 7.

### 5.2 Preliminary study

The first presented analysis regards a comparison study between the meshless method and the FEM. The previously described 2D model is analysed considering the material properties suggested in the literature [48], which are presented in Table 2 for the biologic structures indicated in Figure 5(a).

Table 2: Mechanical properties of the anatomical structures.

Anatomical Structure	Young’s Modulus (GPa)	Poisson’s ratio
Pulp	0.0200	0.45
Dentin	18.6000	0.31
Enamel	41.0000	0.30
Trabecular bone	1.3700	0.30
Cortical bone	13.7000	0.30
Periodontal ligament	0.0689	0.45

In this comparison study the same load suggested in the FEM study [48] is applied: a localized load  $\mathbf{F}_1 = F_0 \cdot \{-\cos \theta, \sin \theta\}$ , being  $F_0 = 100N$  and the angle  $\theta = 22.5 + \alpha_1$ , as indicated in Figure 5(b). In this work, to eliminate local stress concentration, the localized load  $F_1$  was distributed along 5 boundary nodes. The effective stress distribution map obtained with the NNRPIM is presented in Figure 6.

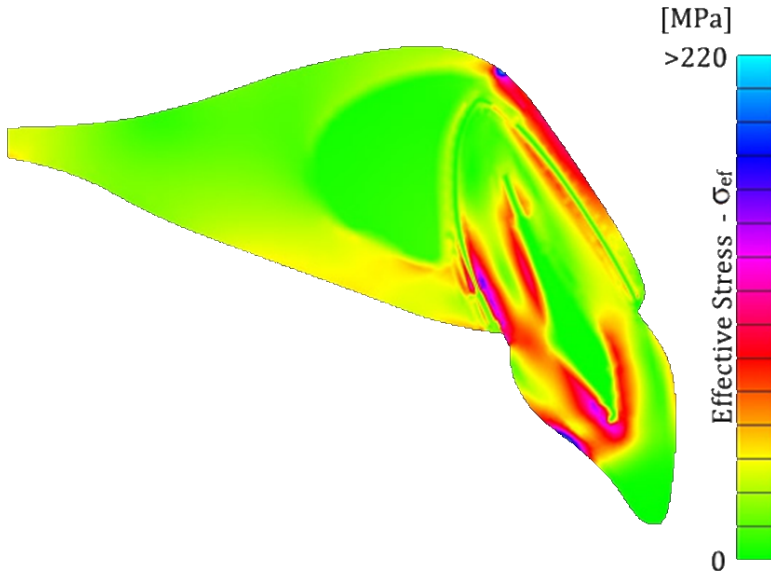


Figure 6: von Mises effective stress field for the first stage of the analysis of the central incisor

Table 3: Maximum principal stress results obtained for the analysis of the central incisor.

$\sigma_1$ (MPa)	Region 1	Region 2	Region 3	Region 4	Region 5	Region 6	Region 7	Region 8
CTRIA3	-9.800	17.000	57.100	-103.000	97.100	-	-	-
CQUAD8	18.400	33.800	68.500	-123.000	138.000	-	-	-
NNRPIM	-12.836	27.672	65.741	-106.688	140.232	-86.753	160.368	-112.633

In Table 3 are presented the maximum principal stress obtained in regions 1 to 8 with the NNRPIM. The meshless results are compared with the results obtained with a 2D linear triangular finite element (CTRIA3) and a quadratic quadrilateral finite element (CQUAD8), [48].

**5.3 Influence of Material Properties**

In this subsection the influence of the considered material mechanical properties is analysed. First, it is studied the influence of the bone tissue mechanical properties on the stress distribution. A literature survey was performed [48,50,51,52,53] and five bone tissue material cases were established, differentiating the cortical and trabecular tissue. The material mechanical properties of the selected bone tissue material cases are presented in Table 4. The numerical model described in the previous subsection was analysed for each bone tissue material case indicated in Table 4. The mechanical properties of all other biologic structures are presented in Table 2. In this analysis the same natural and essential boundary conditions considered in the previous subsection were assumed.

Table 4: Distinct materials properties considered for the bone tissue.

Bone case	Trabecular bone		Cortical bone		reference
	Young’s Modulus E(GPa)	Poisson’s ratio	Young’s Modulus E(GPa)	Poisson’s ratio	
Bone 1	1.00	0.30	13.70	0.30	[50]
Bone 2	1.37	0.30	13.70	0.30	[48]
Bone 3	1.85	0.30	13.70	0.30	[51]
Bone 4	1.85	0.30	14.80	0.30	[52]
Bone 5	3.00	0.30	14.00	0.30	[53]

The obtained von Mises effective stress distribution is presented in Figure 7.

A more detailed examination of the results can be performed through the values presented in Table 5 and Table 6, regarding the von Mises effective stress and the maximum principal stress, respectively.

Next, it is studied the inclusion of restorative materials for the enamel, with the objective to determine which material lead to the most homogeneous stress field. The restorative materials properties were obtained in the literature [11], and are presented in Table 7.

In the present analysis the considered bone tissue material properties are presented in Table 4, identified as “Bone 1”. With the exception of the enamel and the bone tissue material properties, all the other biologic structures identified in Figure 5(a) assume the material properties presented in Table 2. The same 2D model described in previous subsection is considered and the same boundary conditions are imposed. The model was analysed with the NNRPIM considering the four restorative

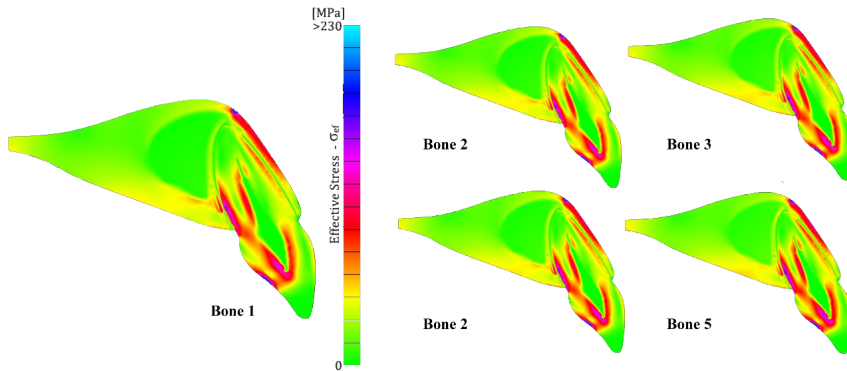


Figure 7: von Mises effective stress field obtained for each distinct bone tissue material case

Table 5: Results of the von Mises effective stress obtained for the distinct regions for each bone case.

$\sigma_{ef}$ (MPa)	Region 1	Region 2	Region 3	Region 4	Region 5	Region 6	Region 7	Region 8
Bone 1	12.875	25.498	66.744	106.545	140.031	86.437	161.031	112.918
Bone 2	12.836	27.672	65.741	106.688	140.232	86.753	160.368	112.633
Bone 3	12.804	29.378	64.715	106.822	140.422	87.084	159.670	112.318
Bone 4	13.259	27.527	65.733	106.516	139.837	87.053	158.603	111.928
Bone 5	12.897	30.697	63.330	106.931	140.533	87.625	158.202	111.652

Table 6: Results of the maximum principal stress obtained for the distinct regions for each distinct bone case.

$\sigma_1$ (MPa)	Region 1	Region 2	Region 3	Region 4	Region 5	Region 6	Region 7	Region 8
Bone 1	-14.666	27.672	69.892	-122.948	146.873	-92.286	158.849	-115.911
Bone 2	-14.618	29.875	68.889	-123.110	147.086	-92.613	158.246	-115.634
Bone 3	-14.578	31.554	67.862	-123.262	147.287	-92.955	157.611	-115.325
Bone 4	-15.113	29.577	69.023	-122.914	146.653	-92.900	156.519	-114.920
Bone 5	-14.682	32.698	66.514	-123.384	147.399	-93.505	156.236	-114.662

Table 7: Mechanical properties of the restorative materials considered.

Crown Material	Young’s Modulus (GPa)	Poisson’s ratio
Gradia Flow	7.40	0.22
Gradia Forte	13.00	0.22
Natural Enamel	41.00	0.30
Feldspathic Ceramics	69.00	0.30

Table 8: Results of the von Mises effective stress obtained for the distinct regions considering distinct crown caps.

$\sigma_{ef}$ (MPa)	Region 1	Region 2	Region 3	Region 4	Region 5	Region 6	Region 7	Region 8
Gradia Flow	13.355	25.302	67.829	66.268	142.594	98.099	170.553	121.449
Gradia Forte	12.989	25.349	67.457	78.195	141.086	94.177	167.604	118.658
Natural Enamel	12.875	25.498	66.744	106.545	140.031	86.437	161.031	112.918
Feldspathic Ceramics	13.031	25.567	66.485	114.700	139.854	83.349	158.392	110.725

Table 9: Results of the maximum principal stress obtained for the distinct regions considering distinct crown caps.

$\sigma_1$ (MPa)	Region 1	Region 2	Region 3	Region 4	Region 5	Region 6	Region 7	Region 8
Gradia Flow	-15.223	27.604	71.049	-70.631	148.187	-103.899	168.413	-124.653
Gradia Forte	-14.789	27.606	70.654	-87.645	147.072	-99.994	165.456	-121.802
Natural Enamel	-14.666	27.672	69.892	-122.948	146.873	-92.286	158.849	-115.911
Feldspathic Ceramics	-14.859	27.713	69.615	-131.736	147.008	-89.200	156.190	-113.654

materials for the enamel presented in Table 7.

In Figure 8 are presented the obtained effective stress maps for the distinct analysis. The local effective stress and the maximum principal stress results obtained for each region indicated in Figure 5(b) are presented respectively in Table 8 and Table 9.

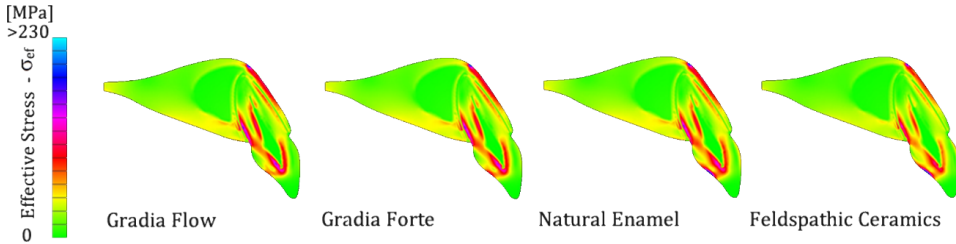


Figure 8: von Mises effective stress field obtained considering distinct materials for the enamel crown

#### 5.4 Maxillary bone tissue remodelling

The model presented in Figure 5 is used to study the bone tissue remodelling process of the maxillary bone supporting the central incisive. The same computational mesh with 4245 nodes, Figure 5(b), is used to discretize the problem domain and the considered mechanical properties for the pulp, dentin, enamel and periodontal ligament are indicated in Table 2. As in previous examples, in the model upper domain boundary the nodal displacements are constrained in both directions, Figure 5(b). Four load cases suggested in the literature [49] are considered in the present analysis, which correspond approximately to the regular solicitation of the incisor due to the daily mastication activity.

The four load cases are localized loads  $\mathbf{F}_i = F_0 \cdot \{-\cos \theta_i, \sin \theta_i\}$ , being the global force  $F_0 = 100N$  and the total angle  $\theta_i = 22.5 + \alpha_i$ , Figure 5(b). Load case 1 is obtained considering  $i = 5$ , load case 2 considers  $i = 4$  and load cases 3 and 4 are obtained considering  $i = 3$  and  $i = 2$  respectively. In this work, to eliminate local stress concentration, all the localized loads  $\mathbf{F}_i$  were distributed along 5 boundary nodes.

For all studied examples, as required by the proposed remodelling algorithm, it is considered an initial uniform density distribution  $\rho_{app}^{max} = 2.1 g/cm^3$  and a Poisson ratio  $\nu = 0.3$ . It is assumed  $\rho_{app}^{control} = 1.0 g/cm^3$  as the remodelling algorithm medium bone density controlled value, which is in accordance with the range of values suggested in the literature [54]. For the parameters from equation (27) ruling

the growth and the decrease of the bone tissue it is considered:  $\alpha = \beta = 0.01$ .

The bone tissue remodelling results are presented with a grey scale, in which the dark-grey colour represents the considered maximum apparent density  $\rho_{app}^{local} = 2.1 \text{ g/cm}^3$  and the light-grey colour represents the minimum apparent density  $\rho_{app}^{local} = 0.1 \text{ g/cm}^3$  admitted. All the other grey tones in the middle represent transitional apparent densities. In each figure presented it is also indicated the bone model medium apparent density, which is obtained applying equation (21). Firstly, each one of the load cases are independently analysed. The results obtained for load case 1 are presented in Figure 9.

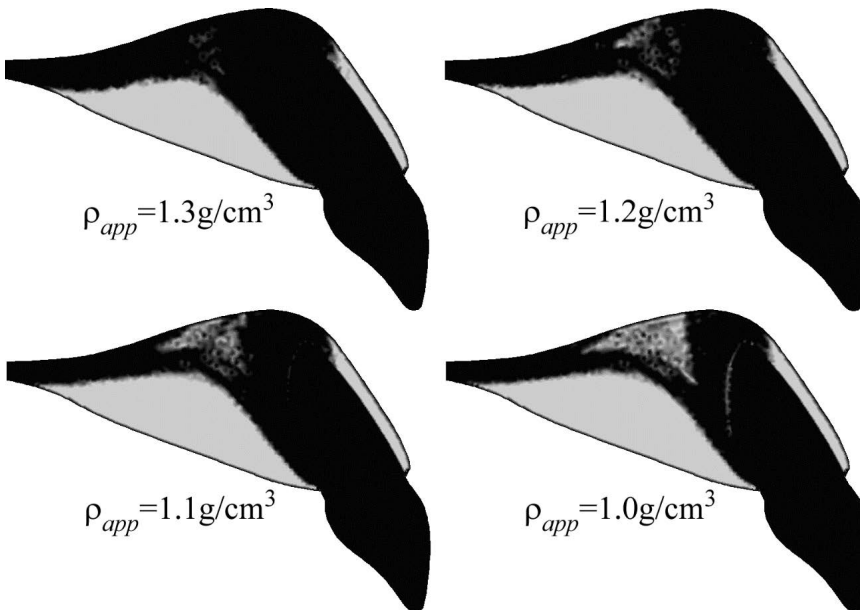


Figure 9: Obtained apparent densities distributions for load case 1 ( $i=5$ ).

It is possible to observe the achieved apparent density distribution for four distinct medium bone densities. The results regarding load cases 2, 3 and 4 are respectively presented in Figure 10, Figure 11 and Figure 12. In each figure are shown four distinct medium bone densities obtained with the respective load case.

In order to obtain a trabecular architecture similar to the real maxillary bone trabecular distribution surrounding the central incisor, it is necessary to consider simultaneously the four load cases. In this study, for each load case, 2500 cycles per day were considered, totalising 10000 masticating movements per day. Notice that in this work the remodelling algorithm weights each load case in the same propor-

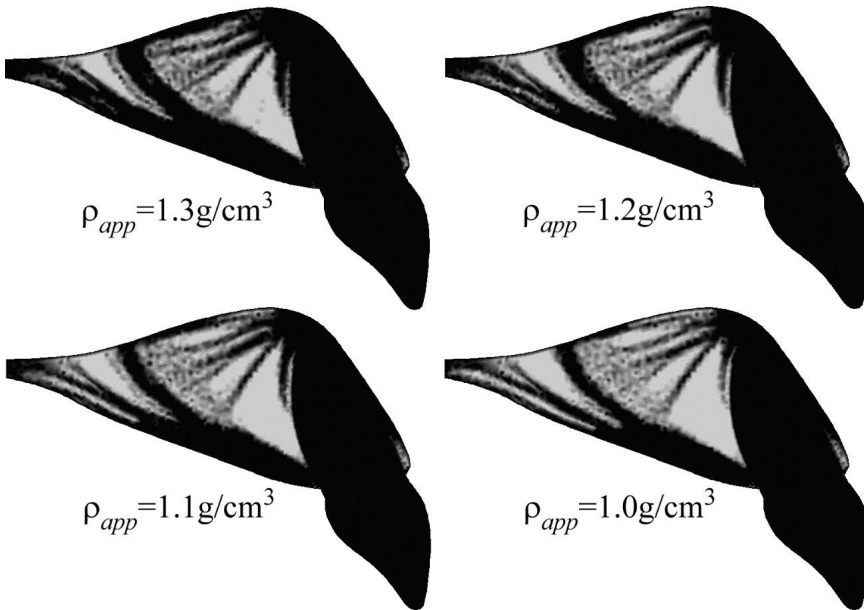


Figure 10: Obtained apparent densities distributions for load case 2 ( $i=4$ ).

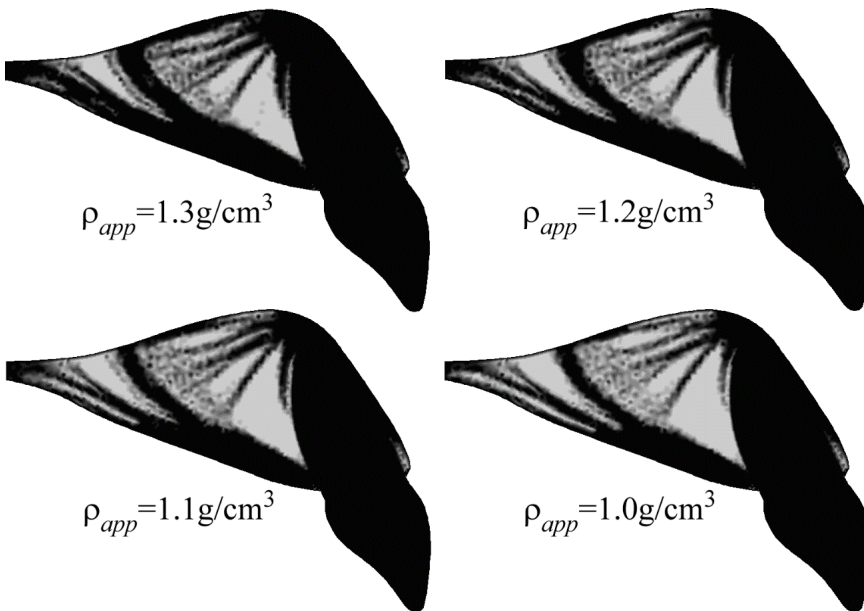


Figure 11: Obtained apparent densities distributions for load case 3 ( $i=3$ ).

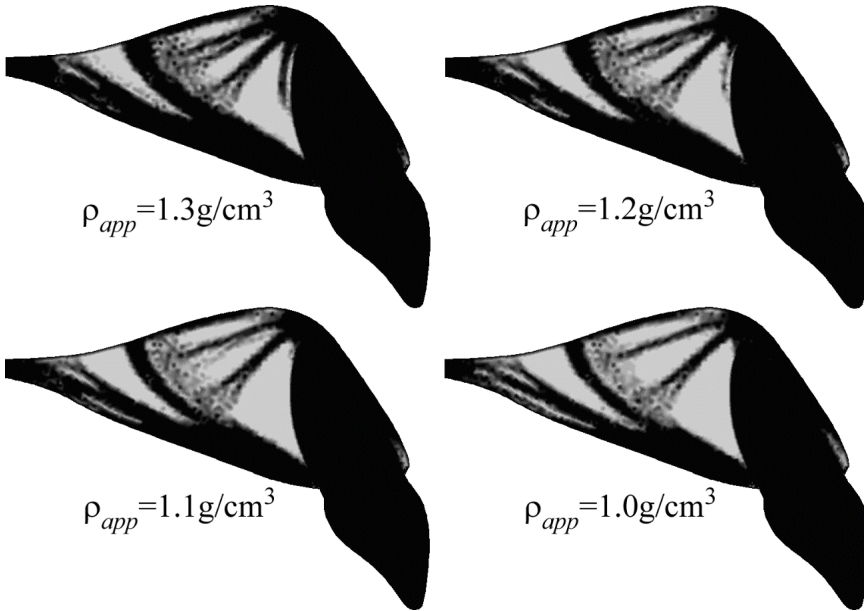


Figure 12: Obtained apparent densities distributions for load case 4 (i=2).

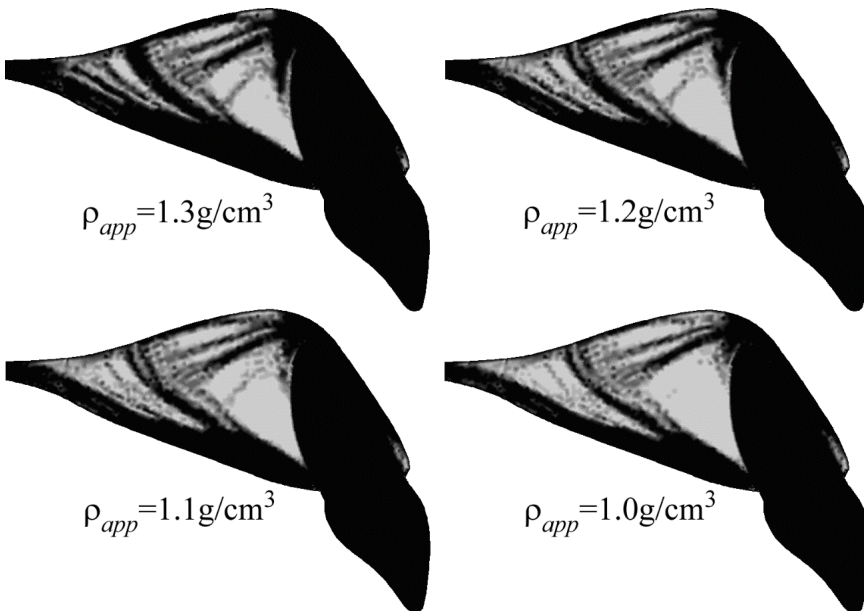


Figure 13: Obtained apparent densities distributions for combination of all load cases.

tion with the number of associated cycles. Thus, in equation (29) it is considered:  $m_i = 2500$  with  $i = \{1, 2, 3, 4\}$ . The results for the four load cases simultaneously applied are presented in Figure 13.

## 6 Discussion

### 6.1 Model limitations

The presented study present some significant limitations. The most evident limitation is the use of a simplified two-dimensional model to simulate a three-dimensional complex biological structure, such is the incisor/maxillary bone system.

Generally, when compared with the FEM, meshless methods are able to produce variable fields more accurately. However, this extra precision comes with a price: a high computational cost, which is mainly due to the large number of nodes required to construct the high-order meshless shape functions and the higher number of integration points needed to integrate the weak form, meshless methods.

Despite being possible to analyse three-dimensional structures using the NNR-PIM [18,29,28], the authors of this work do not possess presently the computational power to analyse a three-dimensional model of the complete teeth and maxillary support bone system, using the same level of discretization used in the two-dimensional model presented in this work.

Since a two-dimensional model is being used, some simplifications had to be made. For instances, all the considered load cases are acting only in the Oxy plane, neglecting any Oz component. Regarding the essential boundary conditions, as suggested in the literature [48], in the model upper domain boundary the nodal displacements are blocked in both directions, aiming to simulate the maxillary immobility, induce by the lack of relative displacements of the maxillary bone with respect to the incisor in the rest position.

### 6.2 Elasto-static analysis

The direct comparison between the stress distribution obtained with the NNRPIM, Figure 6, with the FEM results available in the literature [48], permit to confirm that the NNRPIM results are considerably smoother, as it was already theoretically demonstrated in previous NNRPIM works [18].

Regarding the obtained localized stress values, the results presented in Table 3 show that the NNRPIM results are very close to both FEM solutions. Additionally it is important to refer that the NNRPIM solution was obtained with a 4245 nodal mesh and the CTRIA3 FEM and CQUAD8 FEM solutions were obtained with computational meshes with 9259 nodes and 24868 nodes respectively, showing that

the NNRPIM is capable to obtain good results with a lower discretization level.

In this work, the bone surrounding the incisor was analysed in a preliminary step as a homogeneous material with two distinct bone tissues: cortical bone and trabecular bone. Five combinations of bone tissue were analysed. The objective is to analyse the influence of the bone tissue material properties on the incisor/bone biomechanical system.

In Figure 7 it is possible to visualize that the variation of the bone tissue material properties do not produce significant visible changes in the distinct obtained von Mises effective stress fields. Nevertheless, it is interesting to compare in Table 4 the results obtained with the bone tissue material cases: 1, 2, and 3, since within these three material cases the cortical bone maintains the material properties and the trabecular bone varies the material properties. Notice that the increase of the trabecular bone rigidity leads to higher stress values on the periodontal ligament, region 2, and to lower stress values on the incisor neck, region 1 and 3. It was also observed that the variation of the trabecular bone tissue mechanical properties do not seem to induce relevant changes in the obtained stress values for the remaining studied regions. Comparing bone tissue material cases 3 and 4 it is possible to verify that the increase of the cortical bone rigidity leads to higher stress concentration in the incisor neck, region 1 and 3, and to lower stress values on the periodontal ligament, regions 2 and 7. It is also possible to observe in Table 5 and Table 6 that bone tissue material case 1 induces the highest stress values in the incisor neck regions. Additionally, the material properties of bone case 1 are in accordance with the bone tissue material law proposed by Belinha et al. [8,9], equations (16) and (19).

Regarding the comparison analysis between distinct restorative materials for the enamel, which results are presented in Figure 8, Table 8 and Table 9, notice that when restorative materials with higher rigidity are considered for the artificial enamel, lower stress values are obtained in the root/dentine interface, regions 5, 6 and 8, and in the periodontal ligament on region 7. The decrease of the cap rigidity leads to higher stress values in the incisor neck, region 3. The results indicate that restorative material showing a higher elasticity modulus induce higher stress levels in the artificial cap and lower stress levels in all the other biologic structures

### **6.3 Bone tissue remodelling analysis**

After considering simultaneously the four load cases suggested in the literature [49] (assuming for each load case 2500 masticating movements per day), the final solution obtained with the remodelling approach proposed in this work show an apparent similarity with the central incisor sagittal plane CT-scan images, which can be found in the literature [48], Figure 13.

Demonstrating that with the proposed numerical approach it is possible to predict the same trabecular triangular area in the incisor posterior zone and the superior and inferior maxillary cortical layer. These results indicate that the combination of the NNRPIM with the remodelling algorithm permits to achieve the internal trabecular bone structure if the correct mechanical cases are known.

## 7 Conclusions and Final Remarks

In this work an advanced discretization meshless technique, the Natural Neighbour Radial Point Interpolation Method, was extended for the first time to the numerical analysis of the teeth-bone biologic structure. A complete elasto-static analysis of the incisor/maxillary structure using the NNRPIM was studied and afterwards it was analysed the bone tissue remodelling of the maxillary bone in the incisor surroundings. Both analyses used a two-dimensional model of the maxillary central incisor, based on the literature. The results obtained with the NNRPIM were compared with other numerical method solutions available in the literature and with clinical cases.

Regarding the elasto-static analysis, the results permit to conclude that the NNRPIM, when compared with the finite element method (FEM), presents very close results and smoother stress fields.

The elasto-static analysis also permitted to conclude that the increase of the trabecular bone rigidity leads to higher stress values on the periodontal ligament and to lower stress values on the incisor neck. The opposite was verified with the increase of the cortical bone rigidity.

For the restorative material study, it can be concluded that restorative materials showing a higher elasticity modulus induce higher stress levels in the artificial cap and lower stress levels in all the other biologic structures.

In the literature, it is possible to find research works [55] indicating that the bone tissue remodelling process may be triggered by the inflammatory response in the periodontal tissues caused by the application of a mechanical stimulus. Thus, since the bone tissue remodelling responds indirectly to the stress/strain state on the periodontal ligament, it is expected to induce a higher bone tissue remodelling with restorative materials showing lower elasticity modulus.

The used bone tissue remodelling algorithm, which imposes a gradient transition from the initial isotropic cortical assumption to the final anisotropic trabecular arrangement, is simple to apply and depends mainly on the strain deformation energy density (SED) field in each interest point (integration point). The inclusion of the NNRPIM in the remodelling analysis, instead of FEM, is an asset and not just another way to obtain the SED field, since the accuracy of the remodelling algorithm

depends on the accuracy of the used numerical method.

The obtained results show that the proposed bone anisotropic material law permits a gradient transition between the cortical bone stage and the trabecular bone condition. It was also found that the developed remodelling algorithm combined with the NNRPIM accuracy permits to predict correctly the secondary trabecular structures, which are very important in the stability of the principal structures.

**Acknowledgement:** The authors truly acknowledge the funding provided by Ministério da Educação e Ciência, – Fundação para a Ciência e a Tecnologia (Portugal), under grant SFRH/BPD/75072/2010, and by PEst-OE/EME/LA0022/2014 and also to the project “Biomechanics: contributions to the healthcare”, reference NORTE-07-0124-FEDER-000035 co-financed by Programa Operacional Regional do Norte (ON.2 – O Novo Norte), through the Fundo Europeu de Desenvolvimento Regional (FEDER).

## References

1. Quinn, J. B., Quinn, G. D., Kelly, J. R. & Scherrer, S. S. (2005) Fractographic analyses of three ceramic whole crown restoration failures. *Dent. Mater.*, 21, 10, 920–9.
2. Lin, D., Li, Q., Li, W., Duckmanton, N. & Swain, M. (2010) Mandibular bone remodeling induced by dental implant. *J. Biomech.*, 43, 2, 287–93.
3. Wolff, J. (1986) *The Law of Bone Remodelling*. Springer - Verlag (Translated by Maquet P. and Furlong R. from "Das Gesetz der Transformation der Knochen", Hirschwald, 1892), 126.
4. Carter, D. R., Fyhrie, D. P. & Whalen, R. T. (1987) Trabecular bone density and loading history: Regulation of connective tissue biology by mechanical energy. *J. Biomech.*, 20, 8, 785–794.
5. Cowin, S. C., Sadegh, A. M. & Luo, G. M. (1992) An evolutionary Wolff’s law for trabecular architecture. *J. Biomech. Eng.*, 114, 1, 129–36.
6. Pettermann, H. E., Reiter, T. J. & Rammerstorfer, F. G. (1997) Computational simulation of internal bone remodeling. *Arch. Comput. Methods Eng.*, 4, 4, 295–323.
7. Zioupos, P., Cook, R. B. & Hutchinson, J. R. (2008) Some basic relationships between density values in cancellous and cortical bone. *J. Biomech.*, 41, 9, 1961–8.

8. Belinha, J., Natal Jorge, R. M. & Dinis, L. M. J. S. (2012) Bone tissue remodelling analysis considering a radial point interpolator meshless method. *Eng. Anal. Bound. Elem.*, 36, 11, 1660–1670.
9. Belinha, J., Dinis, L. M. J. S. & Natal Jorge, R. M. (2013) A meshless microscale bone tissue trabecular remodelling analysis considering a new anisotropic bone tissue material law. *Comput. Methods Biomech. Biomed. Engin.*, 16, 11, 1170–84.
10. Geng, J. P., Tan, K. B. & Liu, G. R. (2001) Application of finite element analysis in implant dentistry: a review of the literature. *J. Prosthet. Dent.*, 85, 6, 585–98.
11. Sorrentino, R., Aversa, R., Ferro, V., Auriemma, T., Zarone, F., Ferrari, M. & Apicella, A. (2007) Three-dimensional finite element analysis of strain and stress distributions in endodontically treated maxillary central incisors restored with different post, core and crown materials. *Dent. Mater.*, 23, 8, 983–93.
12. De Jager, N., Pallav, P. & Feilzer, A. J. (2005) The influence of design parameters on the FEA-determined stress distribution in CAD-CAM produced all-ceramic dental crowns. *Dent. Mater.*, 21, 3, 242–51.
13. Bathe, K. (1982) *Finite Element Procedures in Engineering Analysis*. New Jersey: Prentice-Hall, Inc., p. 736.
14. Nguyen, V. P., Rabczuk, T., Bordas, S. & Duflot, M. (2008) Meshless methods: A review and computer implementation aspects. *Math. Comput. Simul.*, 79, 3, 763–813.
15. Belytschko, T., Lu, Y. Y. & Gu, L. (1994) Element-free Galerkin methods. *Int. J. Numer. Methods Eng.*, 37, 2, 229–256.
16. Liu, W. K., Jun, S. & Zhang, Y. F. (1995) Reproducing kernel particle methods. *Int. J. Numer. Methods Fluids*, 20, 8–9, 1081–1106.
17. Atluri, S. N. & Zhu, T. (1998) A new Meshless Local Petrov-Galerkin (MLPG) approach in computational mechanics. *Comput. Mech.*, 22, 2, 117–127.
18. Dinis, L. M. J. S., Natal Jorge, R. M. & Belinha, J. (2007) Analysis of 3D solids using the natural neighbour radial point interpolation method. *Comput. Methods Appl. Mech. Eng.*, 196, 13–16, 2009–2028.

19. Liew, K. M., Zhao, X. & Ferreira, A. J. M. (2011) A review of meshless methods for laminated and functionally graded plates and shells. *Compos. Struct.*, 93, 8, 2031–2041.
20. Belinha, J. (2014) *Meshless Methods in Biomechanics - Bone Tissue Remodelling Analysis*, Vol.16 ed. Lecture Notes in Computational Vision and Biomechanics, Springer Netherlands, p. 320.
21. Wang, J. G., Liu, G. R. & Wu, Y. G. (2001) A point interpolation method for simulating dissipation process of consolidation. *Comput. Methods Appl. Mech. Eng.*, vol. 190, no. 45, pp. 5907–5922.
22. Sukumar, N., Moran, B., Yu Semenov, A. & Belikov, V. V. (2001) Natural neighbour Galerkin methods. *Int. J. Numer. Methods Eng.*, 50, 1, 1–27.
23. Idelsohn, S. R., Oñate, E., Calvo, N. & Del Pin, F. (2003) The meshless finite element method. *Int. J. Numer. Methods Eng.*, 58, 6, 893–912.
24. Belinha, J., Dinis, L. M. J. S. & Natal Jorge, R. M. (2013) The natural radial element method. *Int. J. Numer. Methods Eng.*, 93, 12, 1286–1313.
25. Belinha, J., Dinis, L. M. J. S. & Jorge, R. M. N. (2013) Composite laminated plate analysis using the natural radial element method. *Compos. Struct.*, 103, 50–67.
26. Belinha, J., Dinis, L. M. J. S. & Natal Jorge, R. M. (2013) Analysis of thick plates by the natural radial element method. *Int. J. Mech. Sci.*, 76, 33–48.
27. Dinis, L. M. J. S., Natal Jorge, R. M. & Belinha, J. (2008) Analysis of plates and laminates using the natural neighbour radial point interpolation method. *Eng. Anal. Bound. Elem.*, 32, 3, 267–279.
28. Dinis, L. M. J. S., Natal Jorge, R. M. & Belinha, J. (2009) The Radial Natural Neighbours Interpolators Extended to Elastoplasticity, in *Progress on Meshless Methods - Computational Methods in Applied Sciences*, A. J. M. Ferreira, E. J. Kansa, G. E. Fasshauer, and V. M. A. Leitão, Eds. Springer Netherlands, 2009, pp. 175–198.
29. Dinis, L. M. J. S., Natal Jorge, R. M. & Belinha, J. (2009) Large Deformation Applications with the Radial Natural Neighbours Interpolators. *Comput. Model. Eng. Sci.*, 44, 1, 1–34.
30. Dinis, L. M. J. S., Jorge, R. M. N. & Belinha, J. (2009) The natural neighbour radial point interpolation method: dynamic applications. *Eng. Comput.*, 26, 8, 911–949.

31. Dinis, L. M. J. S., Natal Jorge, R. M. & Belinha, J. (2011) Static and dynamic analysis of laminated plates based on an unconstrained third order theory and using a radial point interpolator meshless method. *Comput. Struct.*, 89, 19–20, 1771–1784.
32. Dinis, L. M. J. S., Natal Jorge, R. M. & Belinha, J. (2011) A natural neighbour meshless method with a 3D shell-like approach in the dynamic analysis of thin 3D structures. *Thin-Walled Struct.*, 49, 1, 185–196.
33. Dinis, L. M. J. S., Natal Jorge, R. M. & Belinha, J. (2010) A 3D shell-like approach using a natural neighbour meshless method: Isotropic and orthotropic thin structures. *Compos. Struct.*, 92, 5, 1132–1142.
34. Dinis, L. M. J. S., Natal Jorge, R. M. & Belinha, J. (2010) Composite Laminated Plates: A 3D Natural Neighbor Radial Point Interpolation Method Approach. *J. Sandw. Struct. Mater.*, 12, 2, 119–138.
35. Dinis, L. M. J. S., Jorge, R. M. N. & Belinha, J. (2010) An Unconstrained Third-Order Plate Theory Applied to Functionally Graded Plates Using a Meshless Method. *Mech. Adv. Mater. Struct.*, 17, 2, 108–133.
36. Sibson, R. (2008) A vector identity for the Dirichlet tessellation. *Math. Proc. Cambridge Philos. Soc.*, 87, 01, 151–155.
37. Moreira, S., Belinha, J., Dinis, L. M. J. S. & Natal Jorge, R. M. (2014) Análise de vigas laminadas utilizando o natural neighbour radial point interpolation method. *Rev. Int. Métodos Numéricos para Cálculo y Diseño en Ing.*, 30, 2, 108–120.
38. Wang J. G. & Liu, G. R. (2002) A point interpolation meshless method based on radial basis functions. *Int. J. Numer. Methods Eng.*, 54, 11, 1623–1648.
39. Hardy, R. L. (1990) Theory and applications of the multiquadric-biharmonic method 20 years of discovery 1968–1988. *Comput. Math. with Appl.*, 19, 8–9, 163–208.
40. Golberg, M. A., Chen, C. S. & Bowman, H. (1999) Some recent results and proposals for the use of radial basis functions in the BEM. *Eng. Anal. Bound. Elem.*, 23, 4, 285–296.
41. Carter, D. R. & Hayes, W. C. (1977) The compressive behavior of bone as a two-phase porous structure. *J. Bone Joint Surg. Am.*, 59, 7, 954–62.

42. Carter, D. R. & Spengler, D. M. (1978) Mechanical properties and composition of cortical bone. *Clin. Orthop. Relat. Res.*, 135, 192–217.
43. Gibson, L. J. (1985) The mechanical behaviour of cancellous bone. *J. Biomech.*, 18, 5, 317–328.
44. Goldstein, S. A. (1987) The mechanical properties of trabecular bone: Dependence on anatomic location and function. *J. Biomech.*, 20, 11–12, 1055–1061.
45. Rice, J. C., Cowin, S. C. & Bowman, J. A. (1988) On the dependence of the elasticity and strength of cancellous bone on apparent density. *J. Biomech.*, 21, 2, 155–168.
46. Martin, R. B. (1991) Determinants of the mechanical properties of bones. *J. Biomech.*, 24, 79–88.
47. Lotz, J. C., Gerhart, T. N. & Hayes, W. C. (1991) Mechanical properties of metaphyseal bone in the proximal femur. *J. Biomech.*, 24, 5, 317–329.
48. Poiate, I. A. V. P., Vasconcellos, A. B., Mori, M. & Poiate, E. (2011) 2D and 3D finite element analysis of central incisor generated by computerized tomography. *Comput. Methods Programs Biomed.*, 104, 2, 292–9.
49. Cheng, R., Zhou, X.-D., Liu, Z. & Hu, T. (2007) Development of a finite element analysis model with curved canal and stress analysis. *J. Endod.*, 33, 6, 727–31.
50. Baggi, L., Cappelloni, I., Maceri, F. & Vairo, G. (2008) Stress-based performance evaluation of osseointegrated dental implants by finite-element simulation. *Simul. Model. Pract. Theory*, 16, 8, 971–987.
51. Meriç, G., Erkmen, E., Kurt, A., Eser, A. & Çelik, G. (2010) Biomechanical evaluation of a fiber-reinforced composite prosthesis supported by implants with and without a microthread collar design. *J. Dent. Sci.*, vol. 5, no. 4, pp. 201–208, Dec. 2010.
52. Meriç, G., Erkmen, E., Kurt, A., Tunç, Y. & Eser, A. (2011) Influence of prosthesis type and material on the stress distribution in bone around implants: A 3-dimensional finite element analysis. *J. Dent. Sci.*, 6, 1, 25–32.
53. Yang, J. & Xiang, H.-J. (2007) A three-dimensional finite element study on the biomechanical behavior of an FGBM dental implant in surrounding bone. *J. Biomech.*, 40, 11, 2377–85.

54. Seong, W.-J., Kim, U.-K., Swift, J. Q., Heo, Y.-C., Hodges, J. S. & Ko, C.-C. (2009) Elastic properties and apparent density of human edentulous maxilla and mandible. *Int. J. Oral Maxillofac. Surg.*, 38, 10, 1088–93.
55. Meeran, N. A. (2013) Cellular response within the periodontal ligament on application of orthodontic forces. *J. Indian Soc. Periodontol.*, 17, 1, 16–20.